Strong Wavelength Detuning of 850 nm Vertical-Cavity Surface-Emitting Lasers for High-Speed (>40 Gbit/s) and Low-Energy Consumption Operation

Kai-Lun Chi, Jia-Liang Yen, Jhih-Min Wun, Jia-Wei Jiang, I-Cheng Lu, Jason Chen, Ying-Jay Yang, and Jin-Wei Shi, *Senior Member, IEEE*

***Abstract*—The strong (>20 nm) wavelength detuning technique has been demonstrated to enhance the modulation speed and high-temperature characteristics (at 85 °C), as well as lower the required driving current density performance of oxide-relief 850-nm vertical-cavity surface-emitting lasers (VCSELs) for >40 Gbit/s operation. By increasing the wavelength detuning from 15 to 20 nm, a significant improvement in the electrical-to-optical (E-O) bandwidth (20 to 27 GHz) of the VCSEL can be observed. This detuning design (∼20 nm) is incorporated along with a Zn-diffusion structure into our oxide-relief VCSEL with a miniaturized oxide-relief aperture (∼3 μm). Highly single-mode, high-speed (26 GHz) operation, and moderate differential resistance (100 Ω) values can be simultaneously achieved. In addition, it is found that devices with a further larger detuning wavelength (>20 nm) and enlarged oxide-relief apertures (∼8 μm) can sustain the same maximum E-O bandwidth (26 GHz) as that of a miniaturized (∼3 μm) VCSEL, resulting in the lower driving current density (8 versus 18.8 kA/cm^2) required for high-speed performance. Excellent transmission performance, which includes an extremely low energy-to-data rate ratio (EDR: 228 fJ/bit; over 100 m OM4 fiber) and record-low driving-current density (8 kA/cm^2; 3.5 mA) has been successfully achieved for 41 Gbit/s error-free transmission for these VCSELs.**

***Index Terms*—Semiconductor lasers, vertical cavity surface emitting lasers.**

I. Introduction

THE optical interconnect (OI) technology has become one of the most important techniques for the construction of the modern cloud infrastructure in the computing industry [1], [2].

Manuscript received January 25, 2015; revised April 9, 2015, May 20, 2015, and June 25, 2015; accepted June 25, 2015. Date of publication June 30, 2015; date of current version August 12, 2015. This work was supported by the Ministry of Science and Technology in Taiwan under Grants MOST 102-2221-E-008-092-MY3 and MOST 103-2622-E-009-004-CC1.

K.-L. Chi, J.-M. Wun, J.-W. Jiang, and J.-W. Shi are with the Department of Electrical Engineering, National Central University, Taoyuan 320, Taiwan (e-mail: porpoise5233@msn.com; p3984011@hotmail.com; ktkvsetko@gmail.com; jwshi@ee.ncu.edu.tw).

J.-L. Yen is with the Department of Information Technology, Takming University of Science and Technology, Taipei 114, Taiwan (e-mail: iamthats@gmail.com;).

I-C. Lu and J. Chen are with the Department of Photonics, National Chiao-Tung University, Hsinchu 300, Taiwan (e-mail: luluso19860219@gmail.com; jchen@mail.nctu.edu.tw).

Y.-J. Yang is with the Department of Electrical Engineering, National Taiwan University, Taipei 106, Taiwan (e-mail: yjyang@cc.ee.ntu.edu.tw).

Color versions of one or more of the figures in this paper are available online at http://ieeexplore.ieee.org.

Digital Object Identifier 10.1109/JSTQE.2015.2451015

Compared with traditional copper cable interconnections, OI can reduce energy consumption, increase the bit-rate-distance product, and save on space, which is important due to the tremendous increase in the bus line density of the rack. Currently, there is competition between two major kinds of OI technologies. One is the 850 nm vertical-cavity surface-emitting lasers (VCSELs) and GaAs photodiode (PD) based transreceiver modules [3], [4], the other is the silicon (Si) photonic platform [1], [5], [6].

Both approaches have been commercially developed for the production of 4×10 Gbit/s active optical cable (AOC)[1,2]. The VCSEL-based multi-mode fiber (MMF) AOC is perhaps more commonly used than the single-mode fiber (SMF) embedded Si photonic platform, because the allowable linking distance (∼300 m) is long enough to satisfy most data center requirements (<50 m) with a much lower energy consumption. Nevertheless, when the data rate reaches ∼50 Gbit/s as expected in the next generation of chip-to-chip OI [7], the Si photonic platform (SiPh[3]) equipped modulator might have a chance to beat the VCSEL based optical engine (MiniPOD[4]) due to its potential electrical-to-optical (E-O) bandwidth, larger than that of the 850 nm VCSEL [1], [5], [6]. Further boosting the speed and reducing the energy consumption of the VCSEL has thus become a major challenge for the next generation of OI applications with data rates at around 50 Gbit/s and a high density of optical bus lines. Recently, transmission data rates as high as 64 Gbit/s over 57 m OM4 multi-mode fibers have been demonstrated by the use of feed forward equalization (FFE) on the transmitter (850 nm VCSELs with 26 GHz bandwidth) and receiver (GaAs p-i-n photodiodes) sides [8]. In addition, energy efficient >40 Gbit/s error-free transmission has also been demonstrated for an 850 nm VCSEL without using an FFE equalizer over MMF [9]–[13].

One possible way to further improve the speed performance and reduce the energy consumption would be to reduce both the parasitic capacitance and driving current by downscaling the diameter of the oxide aperture of the VCSEL (to around 3 μm). A record-low energy-to-data rate ratio (EDR: 56 fJ/bit) has been demonstrated for 850 nm VCESLs with excellent transmission performance at 25 Gbit/s operation [14]. However, there is usually no significant enhancement in the maximum 3-dB electrical-to-optical (E-O) bandwidth of the VCSEL with the decrease in its oxide diameter [11]. This phenomenon might be attributable to the large differential resistance of a VCSEL (∼570 Ω [15])

1077-260X © 2015 IEEE. Personal use is permitted, but republication/redistribution requires IEEE permission.
See http://www.ieee.org/publications_standards/publications/rights/index.html for more information.

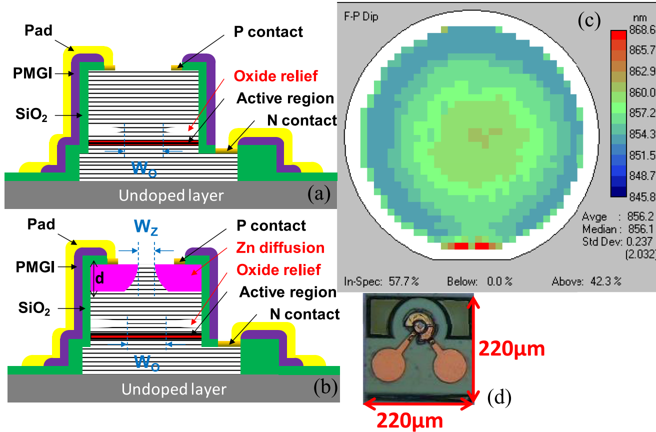

Fig. 1. Conceptual cross-sectional views of (a) devices A to F (without Zn-diffusion) and (b) devices G to O (with Zn-diffusion). (c) FP dips mapping of our VCSEL wafers for device fabrication. (d) Top-view of fabricated VCSEL chip. PMGI: polymethylglutarimide. FP: Fabry-Perot.

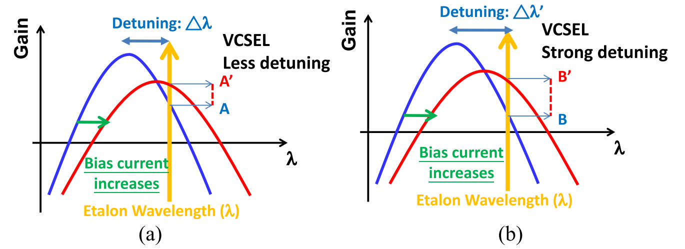

Fig. 2. Conceptual diagram of lasing gain versus wavelength for VCSELs with (a) weak (Δl) and (b) strong ($\Delta\lambda'$) wavelength detuning. AA′ and BB′ represent the increase in gain with the bias current (differential gain) for these two cases. The green arrow represents the red-shift of gain peak with the increase in bias current.

with such a small oxide aperture (2–3 μm) or the single-mode output induced spatial hole burning effect [16], [17]. In addition, the high operating current density ($\sim$43.3 kA/cm^2 [8]; $\sim$25 kA/cm^2 [9], [11], [12]) and the significant stress between the multiple oxide layers and surrounding semiconductor active layers are both issues affecting reliability and performance. The development of a high-speed VCSEL with a moderately large aperture size ($\sim$7 μm), low driving current density (<10 kA/cm^2), and extremely low energy consumption for 50 Gbit/s operations is highly desired for the next generation of inter-chip OIs.

In this study, by adopting strong wavelength detuning (>20 nm) between the peak wavelength of the gain region and the Fabry–Perot (FP) dip in our VCSEL structure, significant enhancement in device modulation speed (20 to 27 GHz), lowering of the threshold current (0.9 to 0.5 mA), and superior high-temperature performance (at 85 °C) are achieved, compared with weaker detuning (15 versus 20 nm). By further incorporating Zn-diffusion and oxide-relief structures [16], [18], [19] into the VCSEL with strong detuning (>20 nm), we obtain a device with moderately large aperture sizes ($\sim$8 μm), requiring a much lower driving current density (8 versus 18.8 kA/cm^2), while preserving the same maximum high-speed performance ($\sim$26 GHz) as that of VCSELs with a miniaturized oxide-relief aperture ($\sim$3μm). Our device successfully demonstrated excellent transmission performance, which includes an extremely low energy-to-data distance (EDDR) ratio (2.28 fJ/(bit × m) over a 100 m OM4 fiber) for 41 Gbit/s error-free transmission and a record-low required driving-current density (8 kA/cm^2; 3.5 mA).

II. Device Structure and Fabrication

Fig. 1(a) and (b) show conceptual cross-sectional views of the demonstrated oxide-relief VCSEL without and with Zn-diffusion apertures, respectively. With Zn-diffusion apertures in the top p-type DBR layers, we can not only manipulate the number of optical transverse modes inside VCSEL cavity but also reduce the differential resistance [16], [18]. In addition, the oxide layer for current confinement is removed from our oxide-relief structure by using selective wet chemical etching [16], [18]. Due to the lower dielectric constant of air compared with that of the AlO_x layers, there is a demonstrated reduction in the parasitic capacitance and improvement in the VCSEL's speed [16], [18]. The diameters of the Zn-diffusion (W_Z) and oxide-relief apertures (W_o) of the measured devices are specified in the figures below. In this work, all the studied devices have fixed values of W_Z and Zn-diffusion depths (d) of $\sim$7 and $\sim$1 μm, respectively. Compared with previous work [16], [18], the thickness of the cavity layer has been further downscaled from 1.5 to 0.5 λ, which shortens the internal carrier transient time [11]. Here, λ is the operating wavelength inside the VCSEL cavity. Due to the increase in the transient-time limited bandwidth, the low-frequency roll-off [16], [17], which is usually the major bandwidth limiting factor of a single-mode VCSEL, can be eliminated; to be discussed in greater detail later. Fig. 1(c) shows the FP dip mapping of the whole of the VCSEL wafer used for device processing. The peak-wavelength of the photoluminescence spectrum of our active layers is at around 838 nm, which indicates that in the center part of our wafer the detuning between the gain peak (838 nm) and FP dip ($\sim$859 nm) can be as large as >20 nm, but this value decreases to around 15 nm in the peripheral part of wafer. Different parts of the wafer are used in the fabrication of VCSELs with different degrees of detuning in order to study its influence on the static/dynamic performance of the VCSELs.

There is a red-shift in the detuning wavelength (FP dip wavelength > gain peak wavelength) because of the significant device self-heating that occurs in our VCSELs with the miniaturized size of cavity under high-speed (high bias current) operation. It would result in the red-shift of the material gain peak. The well-known red-shift detuning technique has been used in VCESLs in order to enhance their high-temperature performance [20], [21]. Fig. 2(a) and (b) shows conceptual diagrams of the gain versus wavelength inside the active layers of VCSEL cavities with weak (Δl) and strong ($\Delta\lambda'$) red-shift wavelength detuning, respectively. Here, the lasing gain distribution related to wavelength is estimated to be parabolic. We can clearly see that the increase in the bias current and elevated junction temperature induce a red-shift and compression of the gain peak, and that the stronger detuning at the etalon wavelength ($\Delta\lambda' > \Delta\lambda$)

can definitely enhance the differential gain ($BB' > AA'$). For the case of the 980 nm VCESL with state-of-the-art high-speed performance at high ambient temperatures [21], the reported value of the thermal resistance (Rth) is around ∼4.7 K/mW, and the corresponding junction temperature is as high as 82 °C under a moderate bias current (∼5.4 mA) and room temperature operation (25 °C) [21]. This helps us to understand the red-shift in the gain spectrum of the VCSEL with the increase in the bias current and red-shift detuning (etalon wavelength > material gain peak wavelength) in VCSELs designed for high-speed performance.

On the other hand, it is well-known that in the edge-emitting distributed feed-back (DFB) laser blue-shift detuning (etalon wavelength < gain peak wavelength of the material) is usually used in order to enhance the modulation speed [22]. The main reason for blue-shift detuning is due to the following. DFB lasers usually have a much smaller value of thermal resistance (0.05 versus ∼4.7 K/mW) than that of the VCSELs, which tends to minimize the device-heating induced bandgap narrowing (red-shift) when the bias current increases [23], [24]. A high-level injection carrier (current) would thus induce a band-filling effect in the active layers of the DFB laser, which would result in the blue-shift in the wavelength of the material gain-peak [22].

As can be seen in Fig. 1(d), the fabricated device has a 26 μm diameter active mesa, which is integrated with the co-planar waveguide (CPW) pads for on-wafer high-speed measurement. The epi-layer structure is grown on a semi-insulating GaAs substrate, which is composed of three $In_{0.15}Al_{0.1}Ga_{0.75}As/Al_{0.3}Ga_{0.7}As$ MQWs sandwiched between a 36-pair n-type and 26-pair p-type $Al_{0.9}Ga_{0.1}As/Al_{0.12}Ga_{0.88}As$ Distributed-Bragg-Reflector (DBR) layers with an $Al_{0.98}Ga_{0.02}As$ layer (50 nm thickness) above the MQWs for oxidation. Compared with that reported for $In_{0.1}Ga_{0.9}As/Al_{0.37}Ga_{0.63}As$ strained 850 nm VCSELs [25], we can achieve a higher indium mole fraction (0.15 versus 0.1) with a thicker well-width (50 versus 40 Å) due to the incorporation of Al, which enlarges the bandgap but has no significant influence on the lattice constant (strain) of the well layer. A thicker well width is usually preferred as beneficial to preserving the uniformity of the VCSEL wafer during material growth. These advantages mean that at a wavelength of ∼ 850 nm, the proposed $Al_xIn_yGa_{1-x-y}As/Al_xGa_{1-x}As$ strained MQW structure can provide a higher indium mole fraction and a wider well-width than those of the $In_xGa_{1-x}As$ based strained 850 nm VCSELs [25], which may further improve their static/dynamic performance.

The influence of wavelength detuning and different sizes of oxide-relief apertures on the dynamic/static performance of the VCSELs is investigated by fabricating devices with different process conditions and geometric sizes. Table I shows details of the key parameters (W_o, W_z, d, and detuning wavelength) of all the devices studied in this paper.

III. Measurement Results

The light output versus current (*L–I*) characteristics of VCSELs with weaker (∼15 nm; devices A to C) and stronger detuning (∼20 nm; devices D to F), are shown in Fig. 3(a) and (b), respectively. Three typical measured traces (devices A to C and D to F) are shown in each figure. The maximum measured 3-dB electrical-to-optical (E-O) bandwidths and corresponding bias currents are also specified. In order to exclude the influence of the optical mode on the device's speed performance [24], the Zn-diffusion apertures have been removed in both structures; conceptual cross-sectional views are shown in Fig. 1(a). In addition, for fair comparison, all these devices have the same size of oxide-relief (current confinement) aperture (6 μm in diameter). As can be seen, devices (D to F) fabricated from the center part of the wafer (stronger detuning) exhibit a lower threshold current (∼0.5 versus ∼0.9 mA) and lower maximum output power (1 versus 2 mW) than do devices (A to C), fabricated from the peripheral part of the wafer. The lower threshold current and smaller maximum power of devices D to F may be attributed to the larger reflectivity of the DBR mirrors in the center part of the wafer, as verified by the measurement results and reflectance spectra mapping across the whole wafer.

Another possible reason for the smaller maximum output power under room temperature operation is the larger misalignment between the gain peak and cavity resonant frequency (FP dip; etalon wavelength) as compared to those of devices A to C. Fortunately, this might not be the most important issue for the applications of inter- or intra-chip OI with a very short-reach linking distance (<50 cm) and negligible optical propagation loss. Figs. 4 and 5 show the measured bias dependent electrical-to-optical (E-O) frequency responses and output optical spectra for devices A and D with weak and strong detuning, respectively. We can clearly see that device D with stronger detuning not has only longer central lasing wavelengths (∼860 versus ∼855 nm) as expected but also a larger maximum 3-dB E-O bandwidth (27 versus 20 GHz).

TABLE I
Gemoetric Sizes and Detuning Wavelengths of the Studied Devices

Device	W_Z (μm)	W_O (μm)	d(μm)	Detuning Wavelength (nm)
A-C	–	6	–	∼15
D-F	–	6	–	∼20
G-I	7	3	1	∼20
J-L	7	6	1	≥20
M-O	7	8	1	≥20

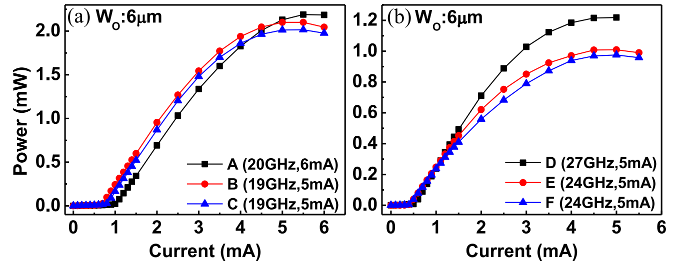

Fig. 3. Measured *L–I* curves of (a) devices A to C (detuning: 15 nm) and (b) devices D to F (detuning: 20 nm). Their oxide-relief apertures (W_o) and measured maximum 3-dB E-O bandwidths and corresponding bias currents are specified.

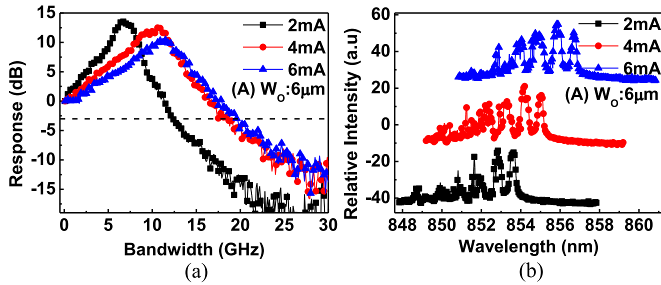

Fig. 4. (a) E-O frequency responses of device A measured under different bias currents and RT operation. (b) The corresponding bias dependent output optical spectra.

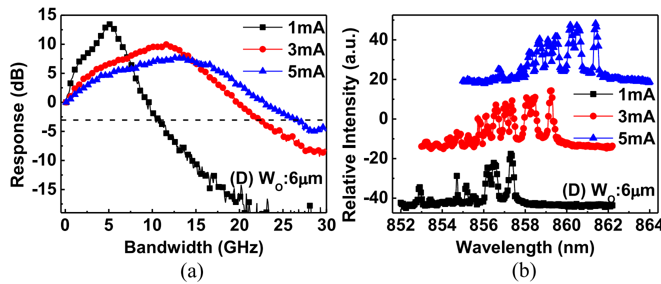

Fig. 5. (a) E-O frequency responses of device D measured under different bias currents and RT operation. (b) The corresponding bias dependent output optical spectra.

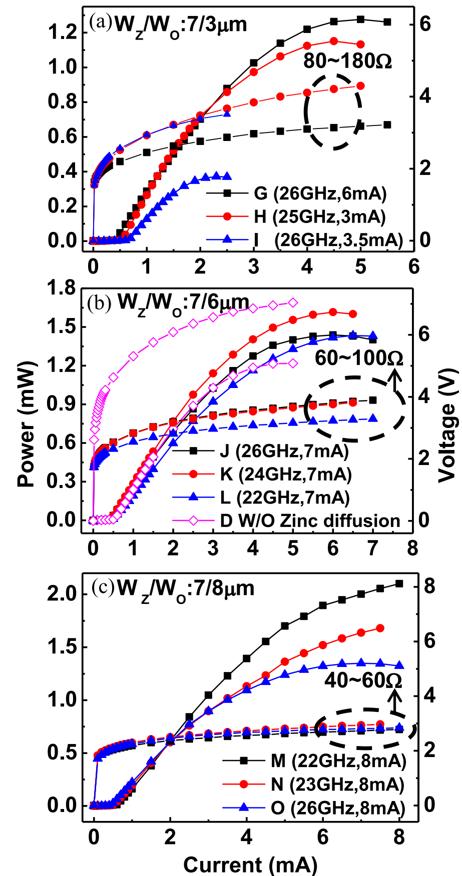

Fig. 6. Measured *L–I–V* curves of VCSELs with oxide-relief apertures of (a) 3 μm (devices G to I), (b) 6 μm (devices J to L), and (c) 8 μm (devices M to O). The range of the measured differential resistance and maximum 3-dB E-O bandwidth with the corresponding bias current of each device is specified. The measured *I–V* curve of device A (without Zn-diffusion) is given in (b) for reference.

The improvement in speed performance of the strong detuning device can be attributed to the enhancement of its differential gain, as illustrated in Fig. 2. In addition, the higher reflectivity of the top DBR mirrors in devices D to F than that of devices A to C might also have an influence on their distinct dynamic performance due to the increase in photon lifetime (τ_p) [26]. A moderate reduction in τ_p will usually result in the enhancement of both the resonant frequency and modulation speed of the VCSEL.

However, if τ_p becomes too small, a significant increase in the threshold current, decrease in the differential gain, and degradation in the modulation speed performance will be observed [26]. A more detailed analysis, which will be presented in a future work, is necessary to investigate whether the lower reflectivity in the top DBR mirrors (smaller τ_p) of devices A to C has a positive or negative effect on their modulation speed.

Data transmission would benefit through further reduction of the differential resistance and manipulation of the optical modes inside the VCSEL cavity [16], [18], [25] through the application of Zn-diffusion apertures in these strong detuning (~20 nm) VCSELs, as shown in the conceptual cross-sectional view in Fig. 1(b). Fig. 6(a) to (c) show the measured *L–I* and *I–V* (voltage) curves of Zn-diffusion devices with three different oxide-relief apertures sizes of 3, 6, and 8 μm, respectively.

Three typical measured traces are shown in each figure. The measured range of differential resistances and maximum E-O bandwidths with corresponding bias currents are also specified. Here, devices G to I, J to L, and M to O have oxide-relief apertures of 3, 6, and 8 μm oxide-relief, respectively. In Fig. 6(b), the measured *I–V* curve (open symbols) for the reference VCSEL (device A) without Zn-diffusion apertures is also included for comparison. As can be seen, there are some variations on the measured differential resistance and voltage drop of these devices, which can be attributed to process variations. These include the uncertainty of the surface state during the p- and n-type Ohmic contact metallization and the uniformity during the wet oxidation processes. Besides, as shown in Fig. 6(b), our Zn-diffusion technique can greatly reduce both the turn-on voltage and differential resistance in the structure with the same-sized oxide-relief apertures (6 μm).

As compared to the *I–V* curves reported for Zn-diffusion VCSELs in our previous work [27], the measured turn-on voltages in this work are usually larger (~2 versus ~1.5 V) and the improvement in *I–V* performance after performing the Zn-diffusion process is more significant. This may be attributed to the elimination of the $Al_x Ga_{1-x} As$ graded bandgap layer (x: 0.6 to x: 0.3) in our new λ/2 cavity layer design, which increases the effective barrier-height. A higher bias voltage is thus necessary to turn on devices. The smaller differential resistance leads to less device-heating and a higher saturation power (~1.3 versus ~1 mW) and bias current (~6 versus ~4 mA), as shown in Figs. 3(b)

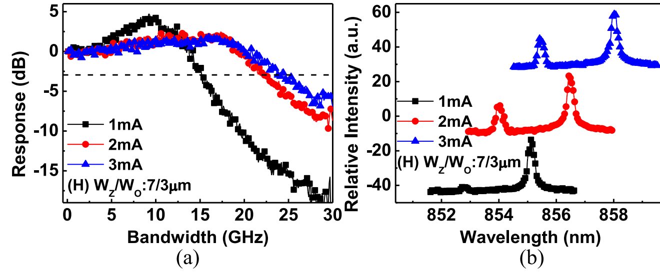

Fig. 7. (a) E-O frequency responses of device H measured under different bias currents and RT operation. (b) The corresponding bias dependent output optical spectra.

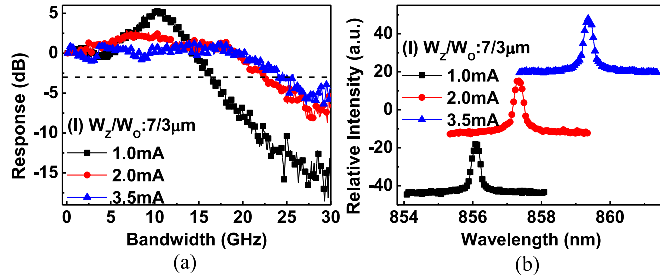

Fig. 8. (a) E-O frequency responses of device I measured under different bias currents and RT operation. (b) The corresponding bias dependent output optical spectra.

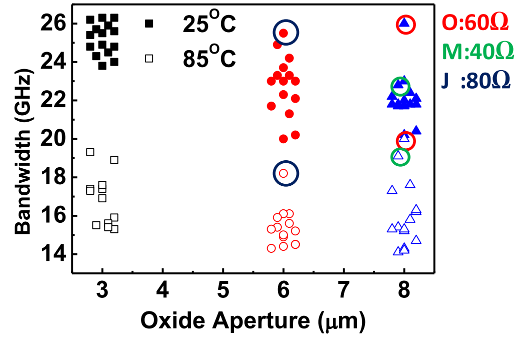

Fig. 9. Measured 3-dB E-O bandwidths of VCSELs with three different oxide-relief apertures under RT (solid symbols) and 85 °C (open symbols) operation.

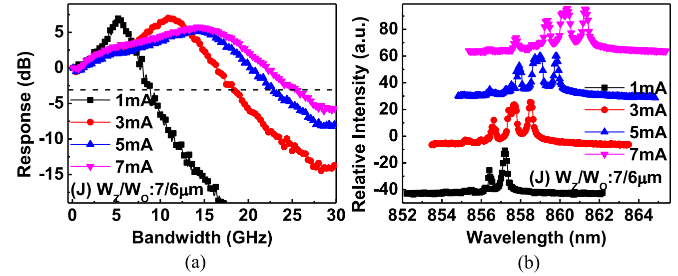

Fig. 10. (a) E-O frequency responses of device J measured under different bias currents and RT operation. (b) The corresponding bias dependent output optical spectra.

and 6(b). Furthermore, as shown in Fig. 6(a), even with a small oxide-relief aperture (3 μm), the measured differential resistance (at ∼5 mA) can be as low as 80 Ω (device G). This is much smaller than the values typically reported (>150 Ω) for high-speed VCSELs at 850 nm with a similar size of current-confined aperture [9]–[13]. Figs. 7 and 8 respectively show the measured bias dependent (E-O) frequency responses and output optical spectra of devices H and I with the same 3 μm current-confined aperture. We can clearly see that (quasi-) single-mode performance can be achieved with a 3-dB E-O bandwidth as wide as 26 GHz under a very low bias current (∼3.5 mA). The low-frequency roll-off problem, which is usually observed in the single-mode 850 nm VCSELs [15]–[17] due to spatial hole burning effect, has been completely removed in our device. This is because the short cavity length (λ/2) design can effectively reduce the supplementary (transient) time of hole injection to the lasing region inside the active layers. We achieved a 3-dB E-O bandwidth (26 GHz) for device I, with a reasonable value of differential resistance (∼100 Ω). This is a record high value among all those reported for 850 nm single-mode VCSELs [9]–[13], [15], [28].

Comparison to the reference VCSEL (device D without Zn-diffusion apertures as illustrated in Fig. 2(b)), there is no significant improvement in the achieved maximum bandwidth (27 versus 26 GHz) after performing the Zn-diffusion process. However, the much narrower spectral width and lower differential resistance of our Zn-diffusion VCSEL does greatly enhance the maximum allowable linking distance [16], [28] and minimize the degradation in measured eye-patterns due to undesired microwave reflection [13], (impedance mismatch between the device and integrated 50 Ω laser driver). These are both important issues for practical applications of VCSELs for data transmission.

As shown in Fig. 6, the increase in the oxide-relief aperture would result in a reduction of the differential resistance, an increase in the output optical power, and degradation in speed performance. The latter is usually observed in large aperture size VCSELs due to an increase in the parasitic capacitance and decrease in the carrier (photon) density. The solid symbols in Fig. 9 represent the summarized results of measured E-O bandwidths for several devices with three different oxide-relief diameters (3, 6, and 8 μm) under room-temperature (RT) operation. As can be seen, there is a gradual improvement in the bandwidths of most devices from 22 to 25 GHz with a downscaling of the size of the oxide-relief apertures from 8 to 3 μm. However, as indicated by the black and red circles, a few devices (devices J and O), even with oxide-relief apertures as large as 6 to 8 μm, can still sustain the same maximum electrical-to-optical (E-O) bandwidth (∼26 GHz) as can the 3 μm aperture devices.

Fig. 10 shows the measured bias dependent E-O frequency responses and output optical spectra of device J with a 6 μm current-confined aperture. We can clearly see that under a bias current of 7 mA bias, a 3-dB E-O bandwidth as wide as ∼26 GHz can still be achieved. This indicates that our devices can be operated under an extremely low driving current density (< 7 mA (<24.8 kA/cm^2)) for > 40 Gbit/s transmission. Having a low operating current density (< 10 kA/cm^2) is a prerequisite for

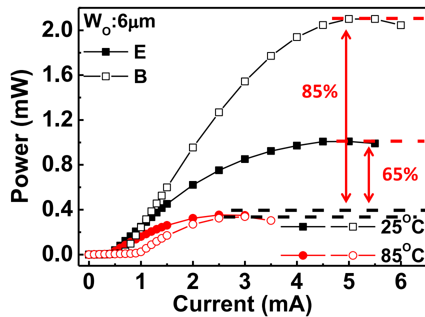

Fig. 11. *L–I* curves of devices B (15 nm detuning) and E (20 nm detuning) measured under 25 °C (RT) and 85 °C operation.

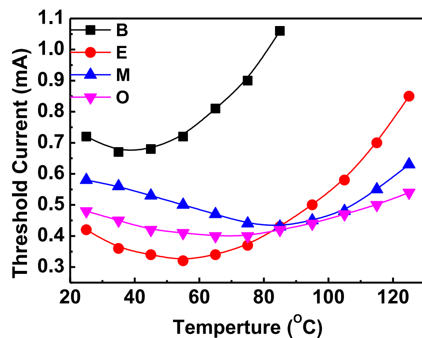

Fig. 12. Measured I_{th} versus ambient temperature of devices B, E, O, and M.

reliable operation and long device lifetime for commercial applications of VCSELs [11], [29]. The measurement results show (see Fig. 9), that device O, which has an oxide-relief diameter as large as 8 μm and high-speed performance (26 GHz), meets these requirements. In the next section, we will discuss the mechanism behind the capability for high-speed operation even with such a large active diameter (∼8 μm) based on the high-temperature (85 °C) static/dynamic measurement results.

The performance of VCSELs under high ambient temperature operation (70 to 85 °C) is an important issue due to the tremendous increase in bus line density of the modern optical rack which will result in worse device heat-sinking. The proposed detuning technique should be of benefit to the high-temperature performance of such devices, as indicated by the red-shift of the gain peak under high ambient temperature operation. Fig. 11 shows the *L–I* curves measured at RT and 85 °C of devices with 15 (B) and 20 (E) nm detuning, respectively; see Fig. 2.

As can be seen, although the strong detuning device E shows a poorer *L–I* curve under RT operation than that of device B, its high-temperature performance is superior. This includes a smaller increase in the threshold current and less degradation in the maximum output power at 85 °C operation (65% versus 85%). Fig. 12 shows the measured I_{th} versus ambient temperature of several devices with strong and weaker detuning. We can clearly see that each trace fits a parabolic function very well, and there is much less variation in the measured threshold currents for the devices (E, M, and O) with strong detuning than that of weak detuning device (B). The measurement results are consistent with the previous discussion; see Figs. 3 to 5. Furthermore, the measured traces of devices O and M show a minimum value of I_{th} at a higher elevated temperature (∼80 °C versus ∼60 °C). The implication is that larger wavelength detuning (>20 nm) occurs in devices M and O compared to device E, as specified in Table I. Fig. 13(a) and (b) show the measured bias dependent E-O frequency responses of device E under RT and 85 °C operation, respectively. As can be seen, for 85 °C operation, the measured E-O bandwidth becomes saturated at a bias current as low as 2 mA and further increase in the bias current (∼3 mA) would lead to a significant degradation in the E-O bandwidth. This can be attributed to the large differential resistance which would induce serious device heating and degradation in speed performance.

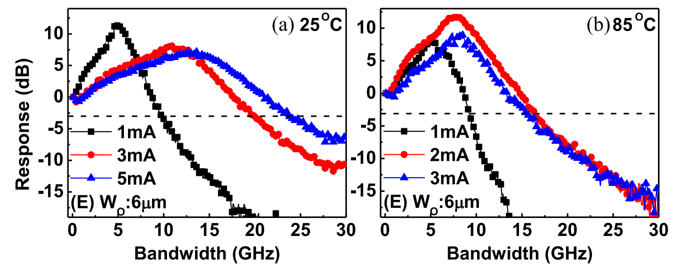

Fig. 13. Bias dependent E-O frequency responses of device E measured under (a) RT and (b) 85 °C operation.

As can be seen in Fig. 6, the Zn-diffusion process can significantly reduce the differential resistance of the device, which would be of benefit to its high-temperature static/dynamic performance.

Fig. 14 shows the *L–I* performance measured under RT and 85 °C operation of VCSELs H, J, L, O, M, fabricated with the Zn-diffusion process and different sized oxide-relief apertures. Comparison to the measurement results for device E in Fig. 11 clearly shows that larger saturation bias currents (∼3.5 versus ∼ 2.5 mA) and power (0.4 versus 0.3 mW) are obtained under 85 °C operation for the VCSELs (device J or L) with the additional Zn-diffusion region and the same size of oxide-relief aperture (6 μm). The *L–I* performance of devices J and O with the fast (∼26 GHz) modulation speed (indicated by the black and red circles in Fig. 9, respectively), and devices L and M with the relatively slow (22–23 GHz) speed performance are both given for comparison in Fig. 14(b) and (c). We can clearly see that although the fast devices (J and O) exhibit a smaller output power than that of the slow devices (L and M) under RT operation, they show less degradation in maximum output when the ambient temperature reaches 85 °C. These results are consistent with the measurement results shown in Fig. 12. Under 85 °C operation, the junction temperature should be much higher due to the serious device self-heating effect in VCSEL; see Fig. 2. We can clearly see that compared with device M, device O suffers a smaller increase in the threshold current (gain) when the temperature exceeds 85 °C. The less degradation in maximum output power performance under high-temperature operation of device O, in comparison with device M, can thus be understood. These measurement results imply that the fast

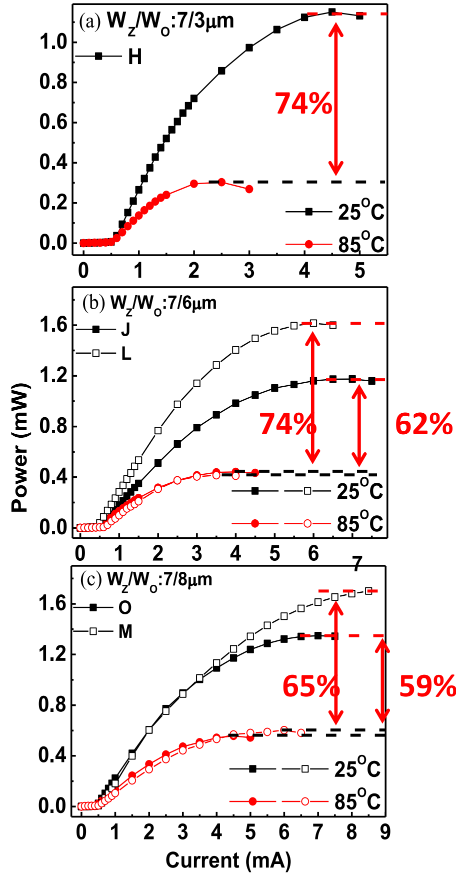

Fig. 14. *L–I* curves of VCSELs measured at RT and 85 °C for devices with oxide-relief apertures of (a) 3 μm (device H), (b) 6 μm (devices J and L), and (c) 8 μm (devices M and O).

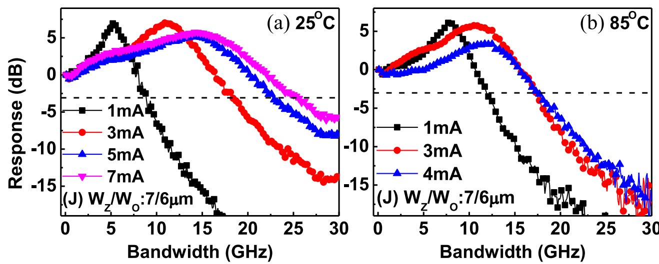

Fig. 15. Bias dependent E-O frequency responses of device J measured under (a) RT and (b) 85 °C operation.

device O may have a larger detuning wavelength, which would result in the higher differential gain (see Fig. 2) than those of the slow devices (L and M). Such variation in the differential gain and detuning wavelength across the same chip may be attributed to fluctuation in the composition of the MQWs (material gain peak wavelength) across the whole wafer.

Figs. 15 and 16 show the bias dependent E-O frequency responses measured under RT and 85 °C operation of devices J and O with the same Zn-diffusion apertures (7 μm) and different sized oxide-relief apertures of 6 and 8 μm, respectively. We can clearly see that both structures can sustain nearly 20 GHz 3-dB E-O bandwidth under 85 °C operation. Such a bandwidth

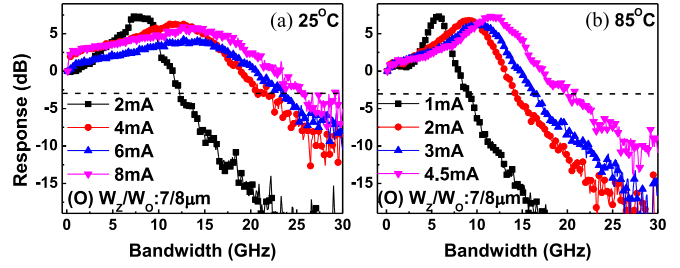

Fig. 16. Bias dependent E-O frequency responses of device O measured under (a) RT and (b) 85 °C operations.

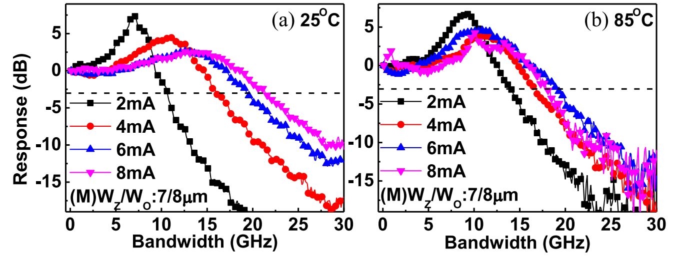

Fig. 17. Bias dependent E-O frequency responses of device M measured under (a) RT and (b) 85 °C operation.

is high enough for 40 Gbit/s transmission under 85 °C operation. Comparison with the measured E-O frequency response of device E, shown in Fig. 13, clearly shows that the measured E-O bandwidth of a device with the additional Zn-diffusion aperture but the same oxide-relief aperture would become saturated at a higher bias current ($\sim$4 versus $\sim$2 mA) with a higher maximum bandwidth (18 versus 16 GHz).

We can thus conclude that for high ambient temperature operation, our Zn-diffusion process can really reduce the differential resistance, minimize device-heating, and benefit both the speed and power performance. Fig. 17 shows the bias dependent E-O frequency responses of device M measured under RT and 85 °C operation. This figure also lends support to the conclusion that the value of the differential resistance play an important role in the dynamic performance of a device under 85 °C operation.

Comparison with the data for device O shown in Fig. 16, indicates that although device M has poorer speed performance under RT operation (22 versus 26 GHz), as a consequence of the smaller differential gain (less detuning wavelength), illustrated in Fig. 14, it can sustain a similar high-speed performance under 85 °C operation ($\sim$20 GHz), due to its smaller differential resistance (40 versus 60 Ω), as specified on Fig. 9. From Figs. 16(b) and 17(b) we can clearly see that the lower differential resistance of device M allows higher current injection (6 versus 4.5 mA) with less device self-heating than for device O. This further boosts the speed performance of device M under high temperature operation. The open symbols in Fig. 9 indicate the summarized 3-dB E-O bandwidths obtained under 85 °C operation for VCSELs with three different sized oxide-relief apertures (3, 6, and 8 μm). As can be seen, some of the 6 and 8 μm devices (J, O, and M), indicated by the black, red, and green circles, respectively, have slightly better speed performance under 85 °C

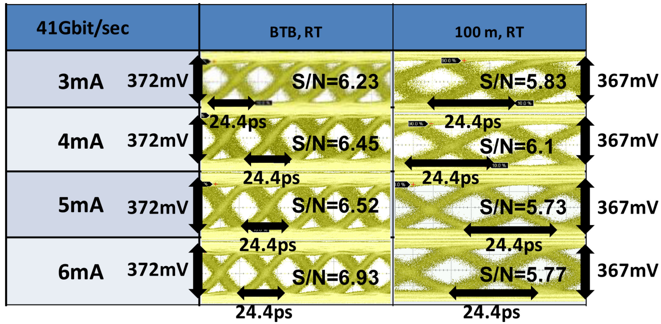

Fig. 18. Measured 41 Gbit/s eye-patterns of device O under different bias currents at RT (BTB and 100 m transmission)

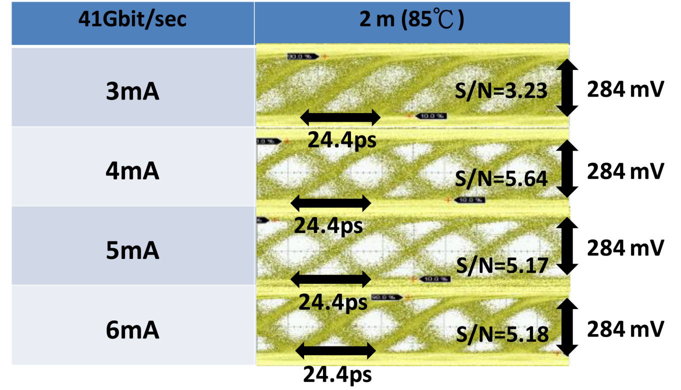

Fig. 19. Measured 41 Gbit/s eye-patterns of device O under different bias currents at 85 °C (2 m transmission)

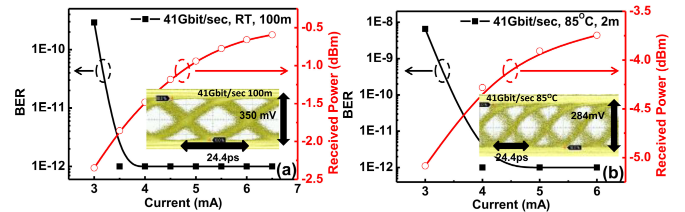

Fig. 20. Measured 41 Gbit/s BER values (in log scale) versus bias current and received optical power of device O at (a) RT over 100 m and at (b) 85 °C over 2 m OM4 fibers.

operation than do the 3 μm devices. This might be attributable to the lower differential resistance among these measured devices.

Fig. 18 shows the measured 41 Gbit/sec eye-patterns of device O for back-to-back (BTB) and over 100 m OM4 fiber cases. The 3-dB E-O bandwidths measured under RT and 85 °C operation are 26 and 20 GHz, respectively, as illustrated in Fig. 16. In our setup for data transmission, the receiver-end is comprised of a commercial photoreceiver (VI-Systems R40–850 photoreceiver), which has a 30 GHz 3-dB O-E bandwidth and good performance for >40 Gbit/s eye-detection [9], [11], [12], [19]. The length and amplitude (V_{pp}) of the electrical pseudorandom binary sequence (PRBS) patterns used in the transmission experiment are fixed at 2^{15}–1 and 0.4 V, respectively.

When the bias current is over 3 mA, clear 41 Gbit/s eye-opening can be achieved for both cases. The data rate (41 Gbit/s) is limited by the maximum data rate of the pulse pattern generator system used here but a further increase in the transmission data rate of up to 50 Gbit/s is highly possible due to the wide E-O bandwidth (26 GHz) of our device [9]. In the case of BTB transmission, we can clearly see that an increase in the bias current would result in enhancement of the S/N ratio of the received eye-pattern. In contrast, in the case of 100 m OM4 fiber transmission, the optimum bias current for best eye-quality is ∼4 mA. A further increase in the bias current would broaden the optical spectral width, inducing more serious modal dispersion, leading to degradation of the S/N ratio of eye-patterns [18].

This suggests that it is the optical spectral width rather than the output power that dominates the transmission performance of the proposed VCSEL for such a short-reach distance (100 m) with negligible transmission loss.

Fig. 19 shows the 41 Gbit/s eye-patterns measured at 85 °C with a 2 m OM4 fiber transmission distance. We can clearly see that 41 Gbit/s error-free eye-opening can still be sustained when the bias current is over 4 mA. The limited transmission distance at 85 °C can be attributed to vibration of the lens fiber used for collection of the output light, which becomes more serious with an increase in the ambient temperature, leading to degradation in the measured eye-pattern quality. A red-shift in the central wavelength and variation in the output optical mode spectrum could also be possible reasons for degradation in the transmission distance under 85 °C operation. However, by the use of robust device packaging, a further improvement in high-temperature transmission performance can be expected.

Fig. 20(a) and (b) show the bit-error-ratio (BER) values versus bias current and received optical power of our device at 41 Gbit/s operation measured under RT and 85 °C transmission, respectively. The corresponding error-free eye-patterns are also specified. Under RT operation, the EDR for 100 m OM4 fiber transmission can be as low as 228 fJ/bit (3.5 mA), which is higher than the lowest EDR value (∼167 fJ/bit) reported for error-free 40 Gbit/s transmission for an 850 nm VCSEL across a shorter MMF (50 m) and under a close value of bias current ∼3.1 mA [12]. The slightly poorer EDR performance of our device is mainly due to the larger turn-on voltage (2 versus 1.5 V) than that of the typical 850 nm VCSEL; see Fig. 6.

Furthermore, thanks to the strong wavelength detuning and highly strained MQW design, this device demonstrates a record low driving-current density (∼8 kA/cm^2; 3.5 mA) for >40 Gbit/s error-free transmission over a 100 m MMF fiber [8]–[13]. High-performance 850 nm VCSELs usually need a driving current density >25 kA/cm^2 for >40 Gbit/s transmission over a 50 m MMF [8]–[13].

IV. Conclusion

In conclusion, we observed a significant enhancement in the E-O bandwidth (27 versus 20 GHz), superior high-temperature characteristics (at 85 °C), and lower driving-current (density) in devices fabricated using strong (∼20 nm) wavelength detuning (FP dip > gain peak wavelength) for 850 nm high-speed

VCSELs with oxide-relief current-confined apertures (VCSELs D-F), as compared to reference devices (VCSELs A to C) with less detuning (∼15 nm). By combining Zn-diffusion apertures with strong detuning in the VCSEL, a further improvement in *I–V* performance and narrowing of the optical spectral width can be simultaneously achieved, which is of benefit to high-speed performance at an elevated ambient temperature (85 °C) as well as transmission performance. Highly single-mode (SMSR > 30 dB) and energy-efficient/high-speed (26 GHz at ∼3 mA bias) performance has been demonstrated for devices with miniaturized oxide-relief apertures (∼3 μm). With a further increase in the detuning wavelength (>20 nm) and enlarged oxide-relief apertures (6–8 μm) a few devices can sustain the same maximum 3-dB E-O bandwidth (26 GHz) as VCSELs with miniaturized oxide-relief apertures (∼3 μm). This would lead to an extremely low driving current density for >40 Gbit/s transmission, which is important for obtaining high reliable operation. Devices with a moderate size of current confined aperture (∼8 μm) and strong detuning (>20 nm) have been used to obtain a record-low driving current density (∼8 kA/cm^2) for energy-efficient (228 fJ/bit, 3.5 mA) at 41 Gbit/s transmission over MMF from RT to 85 °C. The proposed VCSEL structure and strong detuning technique are expected to play vital roles in the development of the next generation of inter-chip OIs with a 50 Gbit/s transmission data rate.

Acknowledgment

The authors would also like to thank Andrew Joel of IQE Europe Ltd for his support in the epitaxial layer growth.

References

[1] M. A. Taubenblatt, “Optical interconnects for high-performance computing,” *J. Lightw. Technol.*, vol. 30, no. 4, pp. 448–458, Feb. 2012.

[2] D. Bimberg, “Green data and computer communication,” presented at the IEEE Photon. Soc. Meet., Arlington, VA, USA, Oct. 2011, Paper TuN3.

[3] J. A. Lott *et al.*, “Arrays of 850 nm photodiodes and vertical cavity surface emitting lasers for 25 to 40 Gbit/sec optical interconnects,” *Phys. Status Solidi (C)*, vol. 9, no. 2, pp. 290–293, Feb. 2012.

[4] C. Xie *et al.*, “850 nm VCSEL and PD for ultra high speed data communication over multimode fiber,” *SEI Tech. Rev.*, no. 77, pp. 69–73, Oct. 2013.

[5] R. Soref, “The past, present, and future of silicon photonics,” *IEEE J. Sel. Topics Quantum Electron.*, vol. 12, no. 6, pp. 1678–1687, Nov./Dec. 2006.

[6] M. J. R. Heck *et al.*, “Hybrid silicon photonic integrated circuit technology” *IEEE J. Sel. Topics Quantum Electron.*, vol. 19, no. 4, p. 6100117, Jul./Aug. 2013.

[7] H. Isono *et al.*, “DMT relative cost consideration,” IEEE P802.3bs 400 Gb/s Ethernet Task Force, Norfolk, VA, USA: May 2014. [Online]. Available: http://www.ieee802.org/3/bs/public/14_05/isono_3bs_02_0514.pdf

[8] D. M. Kuchta *et al.*, “64Gb/s Transmission over 57m MMF using an NRZ modulated 850nm VCSEL,” presented at the Optical Fiber Communication Conf. Exhib., San Francisco, CA, USA, Mar.2014, Paper Th3C.2.

[9] P. Westbergh *et al.*, “High-speed oxide confined 850-nm VCSELs operating error-free at 40 Gb/s up to 85,” *IEEE Photon. Technol. Lett.*, vol. 25, pp. 768–771, Apr. 2013.

[10] P. Westbergh *et al.*, “High-speed 850 nm VCSELs with 28 GHz modulation bandwidth operating error-free up to 44 Gbit/s,” *Electron. Lett.*, vol. 48, no. 18, pp. 1145–1147, Aug. 2012.

[11] P. Moser *et al.*, “Energy-efficient oxide-confined high-speed VCSELs for optical interconnects,” *Proc. SPIE*, vol. 9001, pp. 900103-1–900103-8, Feb. 2014.

[12] P. Wolf *et al.*, “Energy efficient 40 Gbit/s transmission with 850 nm VCSELs at 108 fJ/bit dissipated heat,” *Electron. Lett.*, vol. 49, no. 10, pp. 666–667, May, 2013.

[13] P. Westbergh *et al.*, “High-speed 850 nm VCSELs with 28 GHz modulation bandwidth for short reach communication,” *Proc. SPIE,*, vol. 8639, pp. 86390×1–86390×6, Feb. 2013.

[14] P. Moser *et al.*, “56 fJ dissipated energy per bit of oxide-confined 850 nm VCSELs operating at 25 Gbit/s,” *Electron. Lett.*, vol. 48, no. 20, pp. 1292–1294, Sep. 2012.

[15] P. Moser *et al.*, “81 fJ/bit energy-to-data ratio of 850 nm vertical-cavity surface-emitting lasers for optical interconnects,” *Appl. Phys. Lett.*, vol. 98, no. 23, pp. 231106-1–231106-3, Jun. 2011.

[16] Jin-Wei Shi *et al.*, “Single-mode, high-speed, and high-power vertical-cavity surface-emitting lasers at 850 nm for short to medium reach (2 km) optical interconnects,” *J. Lightw. Technol.*, vol. 31, pp. 4037–4044, Dec. 2013.

[17] J. S. Gustavsson, A. Haglund, J. Bengtsson, P. Modh, and A. Larsson, “Dynamic behavior of fundamental-mode stabilized VCSELs using shallow surface relief,” *IEEE J. Quantum Electron.*, vol. 40, no. 6, pp. 607–619, Jun. 2004.

[18] J.-W. Shi, J.-C. Yan, J.-M. Wun, J. (J.) Chen, and Y.-J. Yang, “Oxide-relief and zn-diffusion 850 nm vertical-cavity surface-emitting lasers with extremely low energy-to-data-rate ratios for 40 Gbit/sec operations,” *IEEE J. Sel. Topics Quantum Electron.*, vol. 19, no. 2, p. 7900208, Mar./Apr. 2013.

[19] K.-L. Chi *et al.*, “Energy efficient 850 nm vertical-cavity surface-emitting lasers with extremely low driving-current density for >40 Gbit/sec error-free transmissions from RT to 85°C,” presented at the Optical Fiber Communication Conf. Exhib., Los Angeles, CA, USA, Mar. 2015,Paper M2D.6

[20] D. B. Young *et al.*, “Enhanced performance of offset-gain high-barrier vertical-cavity surface-emitting lasers,” *IEEE J. Quantum Electron.*, vol. 29, no. 6, pp. 2013–2022, Jun. 1993.

[21] H. Li *et al.*, “Impact of the quantum well gain-to-cavity etalon wavelength offset on the high temperature performance of high bit rate 980-nm VCSELs,” *IEEE J. Quantum Electron.*, vol. 50, no. 8, pp. 613–621, Aug. 2014.

[22] H. Nishimoto, M. Yamaguchi, I. Mito, and K. Kobayashi “High-frequency response for DFB LD due to a wavelength detuning effect,” *J. Lightw. Technol.*, vol. LT-5, no. 10, pp. 1399–1402, Oct. 1987.

[23] M. Funabashi *et al.*, “Recent advances in DFB lasers for ultradense WDM applications,” *IEEE J. Sel. Topics Quantum Electron.*, vol. 10, no. 2, pp. 312–320, Mar./Apr. 2004.

[24] K. Doi *et al.*, “Thermal analysis of self-heating effect in gaInAsP/InP membrane DFB laser on Si substrate,” presented at the IEEE Photon. Soc. Meet., San Francisco, CA, USA: Sep. 2012, Paper ThO2.

[25] S. B. Healy *et al.*, “Active region design for high-speed 850-nm VCSELs,” *IEEE J. Quantum Electron.*, vol. 46, no. 4, pp. 506–512, Apr. 2010.

[26] P. Westbergh, J. S. Gustavsson, B. Kögel, A. Haglund, and A. Larsson, “Impact of photon lifetime on high-speed VCSEL performance,” *IEEE J. Sel. Topics Quantum Electron.*, vol. 17, no. 6, pp. 1603–1613, Nov./Dec. 2011.

[27] J.-W. Shi, C.-C. Chen, Y.-S. Wu, S.-H. Guol, and Y.-J. Yang, “The influence of Zn-diffusion depth on the static and dynamic behaviors of Zn-diffusion high-speed vertical-cavity surface-emitting lasers at a 850nm wavelength,” *IEEE J. Quantum Electron.*, vol. 45, no. 7, pp. 800–806, Jul. 2009.

[28] R. Safaisini, E. Haglund, P. Westbergh, J. S. Gustavsson, and A. Larsson, “20 Gbit/s data transmission over 2 km multimode fibre using 850 nm mode filter VCSEL,” *Electron. Lett.*, vol. 50, no. 1, pp. 40–42, Jan. 2014.

[29] S. Xie *et al.*, “Reliability and failure mechanisms of oxide VCSELs in non-hermetic environments,” *Proc. SPIE*, vol. 4994, pp. 173–180, 2003.

Kai-Lun Chi was born in New Taipei City, Taiwan Feb. 10, 1988. He is currently working toward the Ph.D. degree in the Department of Electrical Engineering, National Central University, Taoyuan, Taiwan. His current research interests include high-speed optoelectronic device measurement and high-speed VCSELs and LEDs for optical interconnect applications.

Jia-Liang Yen was born in Kaohsiung, Taiwan, on September 20, 1969. He received the M.S. and Ph.D. degrees in electrical engineering from National Taiwan University, Taipei, Taiwan, in 1998 and 2004, respectively. He is currently an Assistant Professor at Takming University of Science and Technology (TMUST), Department of Information Technology, Taiwan. His research interests include cloud computing and artificial intelligence, especially the power control of cloud system.

Jhih-Min Wun was born in Taoyuan, Taiwan, on October 03, 1988. He is currently working toward the Master's degree in the Department of Electrical Engineering, National Central University, Taoyuan, Taiwan. His current research interests include high-speed optoelectronic device measurement.

Jia-Wei Jiang was born in Taichung, Taiwan, on July 11, 1989. He is currently working toward the Master's degree in the Department of Electrical Engineering, National Central University, Taoyuan, Taiwan. His current research interests include mass production of high speed and high reliability VCSELs for application in optical interconnects.

I-Cheng Lu received the M.S. degree in electrooptical engineering from the National Taipei University of Technology, Taipei, Taiwan, in 2010. In 2010, he joined the Institute of Electrooptical Engineering in National Chiao Tung University, Hsinchu, Taiwan, where he is currently working toward the Ph.D. degree. His research interests include advanced modulation formats and short-range optical communications.

Jason (Jyehong) Chen received the B.S. and M.S. degrees in electrical engineering from National Taiwan University, Taipei, Taiwan, in 1988 and 1990, respectively, and the Ph.D. degree in electrical engineering and computer science from the University of Maryland, Baltimore County, MD, USA, in 1998. He joined JDSU in 1998 as a Senior Engineer and received 10 U.S. patents in 2 years. He joined the faculty of National Chiao-Tung University, Taiwan, in 2003, where he is currently a Professor in the Institute of Electro-Optical Engineering and Department of Photonics. He has published more than 100 papers in international journals and conferences. His research interests include hybrid access networks, long reach passive optical networks and optical interconnects.

Ying-Jay Yang was born in I-Lan, Taiwan, in 1952. He received the B.S. degree in electrical engineering from National Taiwan University, Taipei, Taiwan, in 1974, the M.S. and Ph.D. degrees in electrical engineering from North Carolina State University, Rayleigh, NC, USA, in 1982 and 1987, respectively. During his Ph.D. work, he invented the first quantum-well Transverse Junction Stripe (TJS) lasers and also the first CW operation strained-layer TJS lasers. From 1987 to 1989, he was employed as an Engineer at Hewlett Packard, working on the development of 1.3 um InGaAsP LEDs for FDDI. From 1989 to 1993, he joined the Lockheed Palo Alto Research Laboratory as a Research Scientist. He worked on the vertical-cavity surface emitting lasers (SELs), invented the first single transverse mode SELs, and the first optoelectronic integration circuits (OEICs) with an SEL and a FET. In February 1993, he joined the Department of Electrical Engineering, National Taiwan University, where he is currently a Professor. His current research interests include semiconductor materials, and devices including lasers, modulators, quantum devices and OEICs.

Jin-Wei Shi was born in Kaohsiung, Taiwan, on January 22, 1976. He received the B.S. degree in electrical engineering from the National Taiwan University, Taipei, Taiwan, in 1998 and the Ph.D. degree from the Graduate Institute of Electrooptical Engineering, National Taiwan University, Taipei, Taiwan, in 2002. He was a Visiting Scholar at the University of California, Santa Barbara (UCSB), CA, USA, in 2000 and 2001. In 2002–2003, he served as a postdoc at the Electronic Research and Service Organization (ERSO) of the Industrial Technology Research Institute (ITRI). In 2003, he joined the Department of Electrical Engineering, National Central University, Taoyuan, Taiwan, where he is currently a Professor. In 2011, he again joined the ECE Department of UCSB as a Visiting Scholar. His current research interests include ultrahigh speed/power optoelectronic devices, such as photodetectors, electroabsorption modulators, submillimeter wave photonic transmitters, and semiconductor lasers. He has authored or coauthored more than 110 Journal papers, 160 conference papers, and hold 20 patents. He was an Invited Speaker at the 2002 IEEE LEOS, 2005 SPIE Optics East, 2007 Asia-Pacific Microwave Photonic conference (AP-MWP), 2008 Asia Optical Fiber Communication & Optoelectronic Exposition & Conference (AOE), 2011 Optical Fiber Communication (OFC), and 2012 IEEE Photonic Conference (IPC). He served on the technical program committees for the OFC 2009–2011, 2012 SSDM, 2012 MWP, and 2013 Asia-Pacific CLEO. In 2007, he received the Excellent Young Researcher Award from the Association of Chinese IEEE and in 2010 he received the Da-You Wu Memorial Award.